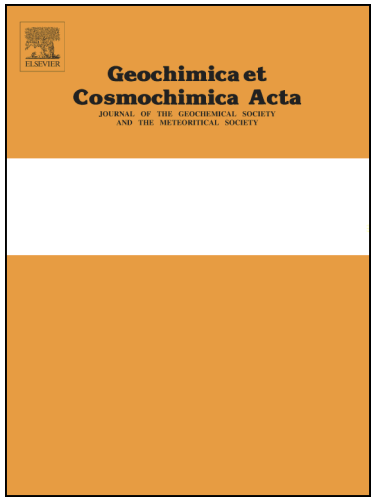

Mid-ocean ridge basalt generation along the slow-spreading, South Mid-Atlantic Ridge (5-11°S): inferences from ^{238}U-^{230}Th-^{226}Ra disequilibria

Simon Turner, Thomas Kokfelt, Folkmar Hauff, Karsten Haase, Craig Lundstrom, Kaj Hoernle, Isobel Yeo, Colin Devey

PII: S0016-7037(15)00480-9
DOI: http://dx.doi.org/10.1016/j.gca.2015.07.036
Reference: GCA 9390

To appear in: *Geochimica et Cosmochimica Acta*

Received Date: 30 October 2014
Accepted Date: 27 July 2015

Please cite this article as: Turner, S., Kokfelt, T., Hauff, F., Haase, K., Lundstrom, C., Hoernle, K., Yeo, I., Devey, C., Mid-ocean ridge basalt generation along the slow-spreading, South Mid-Atlantic Ridge (5-11°S): inferences from ^{238}U-^{230}Th-^{226}Ra disequilibria, *Geochimica et Cosmochimica Acta* (2015), doi: http://dx.doi.org/10.1016/j.gca.2015.07.036

Mid-ocean ridge basalt generation along the slow-spreading, South Mid-Atlantic Ridge (5-11ºS): inferences from ^{238}U-^{230}Th-^{226}Ra disequilibria

Simon Turner [a*], Thomas Kokfelt [b], Folkmar Hauff [c], Karsten Haase [d], Craig Lundstrom [e], Kaj Hoernle [c], Isobel Yeo [c], Colin Devey [c]

[a] *Department of Earth and Planetary Sciences, Macquarie University, Sydney, Australia*

[b] *The National Geological Survey of Denmark and Greenland, 1350 Copenhagen K, Denmark*

[c] *IFM-GEOMAR Helmholtz Centre for Ocean Research Kiel, Wischhofstrasse 1-3, D-24148 Kiel, Germany*

[d] *GeoZentrum Nordbayern, Friedrich-Alexander-Universität Erlangen-Nürnberg, Schlossgarten 5, D-91054 Erlangen, Germany*

[e] *Department of Geology, University of Illinois at Urbana Champaign, IL61801, USA*

* Correpsonding author. Tel.: +61 9850 8636; fax: +61 9850 9102.

E-mail address: simon.turner@mq.edu.au (S. Turner).

Abstract

U-series disequilibria have provided important constraints on the physical processes of partial melting that produce basaltic magma beneath mid-ocean ridges. Here we present the first ^{238}U-^{230}Th-^{226}Ra isotope data for a suite of 83 basalts sampled between 5 and 11ºS along the South Mid-Atlantic Ridge. This section of the ridge can be divided into 5 segments (A0-A4) and the depths to the ridge axis span much of the global range, varying from 1429 to 4514 m. Previous work has also demonstrated that strong trace element and radiogenic isotope heterogeneity existed in the source regions of these basalts. Accordingly, this area provides an ideal location in which to investigate the effects of both inferred melt column length and recycled materials. ^{226}Ra-^{230}Th disequilibria indicate that the majority of the basalts are less than a few millennia old such that their ^{230}Th values do not require any age correction. The U-Th isotope data span a significant range from secular equilibrium up to 32% ^{230}Th excess, also similar to the global range, and vary from segment to segment. However, the ($^{230}Th/^{238}U$) ratios are not negatively correlated with axial depth and the samples with the largest ^{230}Th excesses come from the deepest ridge segment (A1). Two sub-parallel and positively sloped arrays (for segments A0-2 and A3 and A4) between ($^{230}Th/^{238}U$) and Th/U ratios can be modelled in various ways as mixing between melts from peridotite and recycled mafic lithologies. Despite abundant evidence for source heterogeneity, there is no simple correlation between ($^{230}Th/^{238}U$) and radiogenic isotope ratios suggesting that at least some of the trace element and radiogenic isotope variability may have been imparted to the source regions > 350 kyr prior to partial melting to produce the basalts. In our preferred model, the two ($^{230}Th/^{238}U$) versus Th/U arrays can be explained by mixing of melts from one or more recycled mafic lithologies with melts derived from chemically heterogeneous peridotite source regions.

Keywords: South Mid-Atlantic Ridge; basalt; U-series disequilibria; melting dynamics

1. INTRODUCTION

Mid-ocean ridge basalts (MORB) constitute the majority of volcanism on Earth and reflect the simplest scenario whereby melting is a manifestation of adiabatic decompression beneath divergent plates. Because U-series disequilibria in MORB are strongly influenced by melting rate and residual porosity, they have provided unique insights into the physical processes of melting beneath ridges (see Elliott and Spiegelman, 2003, for a summary). For a single lithology (e.g. peridotite), the melting rate should be proportional to the upwelling rate (~ the half spreading rate). Mineral/melt partitioning is also crucial to fractionation of the nuclides involved and in many models U-Th disequilibria are thought to primarily reflect melting within the garnet-stability zone, where Th is significantly more incompatible than U (e.g. Beattie, 1993; Salters and Longhi, 1999; Blundy and Wood, 2003). Some studies have accordingly made links between models in which ridge depth decreases with increasing mantle potential temperature and the overall length of the melting column and evidence that ^{230}Th excess is inversely correlated with ridge depth (e.g. Bourdon et al., 1996a). In contrast, the observation of a negative correlation between ^{226}Ra-^{230}Th and ^{230}Th-^{238}U disequilibria in MORB from the East Pacific Rise (Sims et al., 2002) has led to the development of so-called "two-porosity" models (e.g. Iwamori, 1994; Jull et al., 2002). These emphasise the potential importance of mixing of different melts originating at different depths and having different pathways of extraction within a melting column (one by fast channels and one by slow percolation). However, just how ubiquitous this negative trend between ^{226}Ra-^{230}Th and ^{230}Th-^{238}U is has yet to be established.

At the same time as these developments there has been an increasing awareness of the potential for the presence of recycled, mafic lithologies like pyroxenite or eclogite to exert a major control on U-series disequilibria. These not only have different mineralogy to peridotite (and thus different bulk partition coefficients for U and Th), but also have different (higher) melt productivity per GPa decompression (Hirschmann and Stolper, 1996; Pertermann and Hirschmann, 2003a,b; Pertermann et al., 2004; Kogiso et al., 2004). As a consequence, recycled materials are likely to

78 undergo melting at faster rates that allow less time for radiogenic in-growth. However, this can be
79 offset by the presence of larger amounts of garnet and high-pressure clinopyroxene will result in
80 larger U/Th fractionation than in peridotite. An implicit implication of these models is that there
81 should be a coupling between U-series disequilibria and trace element and radiogenic isotope
82 anomalies (Stracke et al., 1999), unless the influence of the recycled materials is simply to fertilize
83 overlying peridotite > 350 kyr prior to final melting (Prytulak and Elliott, 2009). Finally, the
84 presence of water as a form of "heterogeneity" will result in a deepening of the onset of melting but
85 also a decrease in initial melt productivity thereby increasing the magnitude of resultant ^{230}Th
86 excesses (e.g. Azimow et al., 2004; Bourdon et al., 2006). In this case, there need be no implicit
87 link to radiogenic isotope or trace element signatures.
88 In light of the potential inter-play between the different factors outlined above, many recent
89 studies have focused, but not always reached consensus, upon the relative roles of melt column
90 length and heterogeneities in controlling U-series disequilibria (e.g. Lundstrom et al., 1998, 1999;
91 Sims et al., 2002; Tepley et al., 2004; Russo et al., 2009; Waters et al., 2011; Elkins et al., 2011,
92 2014). To further these investigations, we undertook a detailed study of U-Th-Ra disequilibria from
93 the South Mid-Atlantic Ridge (SMAR). This is a slow-spreading ridge that encompasses much of
94 the global range in ridge depth (1430–4510 m) along which sampled MORB show convincing
95 evidence for contributions from highly heterogeneous mantle sources (Paulick et al., 2010; Hoernle
96 et al., 2011). Thus, it provides an ideal locality in which to investigate the effects of both melt
97 column length and recycled materials. In many respects, our experiment is very similar to the recent
98 study of Elkins et al. (2014) but the results differ in several aspects.
99

100 **2. GEOLOGICAL AND GEOCHEMICAL BACK-GROUND**

101 As illustrated on Fig. 1, the SMAR between the Ascension Fracture Zone (AFZ) and Bode
102 Verde Fracture Zone (BVFZ) can be divided into four segments, based on non-transform
103 discontinuities in the ridge axis. Segments are numbered A1 to A4 going southwards from the AFZ

104 to the BVFZ (Fig. 1A). All samples between 4.8 and 7.6°S are collectively referred to as the A0
105 group, which includes the northernmost sample location of segment A1 (130DS), a small segment
106 within the AFZ and all samples north of the AFZ. Water depths to the ridge axis for the A0, A1 and
107 A4 sample locations are > 2950 meters below sea level and these portions are characterized by deep
108 rift valleys, typical of slow spreading centers. In contrast, segments A2 (2100–3000 meters below
109 sea level) and A3 (~1400–3000 meters below sea level) have rifted axial highs, typical of fast
110 spreading ridges (Bruguier et al., 2003). The decreasing depth (increasing elevation above the
111 surrounding seafloor) of the ridge axis correlates with the crustal thickness and the seafloor
112 morphology, with the thickness increasing from normal thicknesses of ~6 km at segments A1 and
113 A4 to ~ 11 km near a seamount chain extending from the A3 ridge axis to the east (Bruguier et al.,
114 2003; Minshull et al., 1998). Despite the proximity of Ascension Island to the central part of the A1
115 ridge axis (~ 80 km), the depths and morphology of this ridge segment are typical of the SMAR
116 farther north. The full spreading rate along the SMAR between AFZ and BVFZ is 32–33 mm/yr
117 (DeMets et al., 1994). Bathymetric data indicates that the A2 ridge segment has been propagating
118 north for at least the last 4 Ma (Bruguier et al., 2003) whilst combined bathymetric and magnetic
119 data indicate that the A3 ridge segment experienced an eastern ridge jump 1–2Ma ago (Brozena,
120 1986; Bruguier et al., 2003).

121 In terms of geochemical background, all of the samples analysed here are basalts with SiO_2
122 = 46.2 – 52.3 wt. % and MgO = 9.7 – 3.8 wt. %. On a plot of K_2O/TiO_2 x 100 versus SiO_2 the
123 majority of the basalts from segment A0, including the Ascension Fracture Zone (AFZ) samples, as
124 well as those from segments A1 and A4 are NMORB whilst those from segment A3 are EMORB
125 and those from A2 straddle the boundary between the two (Fig. 2A). Almeev et al. (2008)
126 determined that the H_2O contents in the parental melts for the NMORB samples were low (0.04-
127 0.09 wt. %) whereas those from the EMORB were significantly higher at 0.30-0.55 wt. %.

128 Hoernle et al. (2011) showed that trace element indicators for the involvement of enriched
129 components (e.g. chondrite-normalised La/Sm_N, Sm/Yb_N or radiogenic isotopes) do not always

correlate with the depth of the ridge axis and that there are marked maximum anomalies at segments A1 and A3. They also used a plot of $^{143}Nd/^{144}Nd$ versus $^{208}Pb/^{206}Pb$ (reproduced here in Fig. 2B) to argue that the SMAR basalts sampled one depleted and three enriched end-member (HIMU-like) components as follows: the depleted, NMORB source component (DMM) is sampled at segment A0 (including the AFZ samples); segment A1 basalts extend from this to an Ascension Island-like, enriched component which has low $^{143}Nd/^{144}Nd$ and $^{208}Pb/^{206}Pb$ ratios; segment A2 basalts extend towards an enriched component with higher $^{143}Nd/^{144}Nd$ and $^{208}Pb/^{206}Pb$ than the inferred Ascension Island end-member; the basalts from segments A3 extend towards an enriched component that has lower $^{143}Nd/^{144}Nd$ than the inferred Ascension Island end-member and where the basalts from segment A4 cluster with almost no internal variation in Nd or Pb isotopes (see Fig. 2B). Note that in a previous study of the same area, Paulick et al. (2010) used Hf-Nd isotope relationships to argue for two separate depleted end-member components, but only a single, enriched, Ascension Island-like end-member. We did not find evidence for this in our own Hf isotope data.

Lastly, although $^{87}Sr/^{86}Sr$ increases in the order segment A0→A1→A2→A4→A3, there is no correlation between $^{87}Sr/^{86}Sr$ and SiO_2 within each segment nor is there any correlation between SiO_2 and Cl/K as might be expected if differentiation was associated with assimilation of altered oceanic crust or gabbro (e.g. Wanless et al., 2010). Therefore, we attribute the range in trace element and radiogenic isotope ratios to variations in the composition of the sources of the basalts.

3. SAMPLE SELECTION AND METHODS

The 83 samples analysed here were aliquots of the same glasses for which trace element and Sr-Nd-Pb isotope data were presented by (Hoernle et al., 2011). Using those data as a guide, we selected for analysis 5 samples from the A0 and AFZ segments, 13 from segment A1, 31 from segment A2, 25 from segment A3 and 9 from segment A4. Every effort was made to ensure that the samples were taken as close to the centre of the ridge axis as possible and these sampling locations

156 are shown relative to bathymetry on Fig. 1.

157 In order to ensure that the complete dataset is available, we present electron microprobe
158 major element data for all of the glasses analysed here in supplementary Table S1. Those analyses
159 were conducted using a JEOL JXA-8900 electron microprobe at the Institut für Geowissenschaften,
160 Universität Kiel. The instrument was operated at 15 kV acceleration voltage and with a fully
161 focused beam at a current of 12 nA. For calibration and monitoring of data quality, natural and
162 synthetic reference materials from the Smithsonian Institute (Jarosewich et al., 1980) were analysed
163 at the beginning and end of each analytical session.

164 The U-Th-Ra analyses were analysed by thermal ionisation mass spectrometry (TIMS) at
165 GEOMR, Kiel. All work was undertaken on mm-sized glass chips broken of glassy pillow rinds that
166 were hand-picked under a binocular microscope. Typically 0.2-0.7 g of chips were leached for 10
167 min with a 1:1 mixture of 2.5 M HCl and 30 % hydrogen peroxide in an ultra-sonic bath at room
168 temperature and then rinsed several times in Milli-Q water. The data presented here were obtained
169 at the same time as a study of the Galapagos spreading centres by Kokfelt et al. (2005) and so the
170 reader is also referred to that paper for full details of the spiking and chemical separation and
171 analysis procedures. Th measurements followed the ^{229}Th-bridge technique whereby the ^{230}Th/^{232}Th
172 ratio is acquired in two dynamic steps on the RPQ-SEM. We report full internal analytical errors in
173 Table 1 as well as our results for multiple determinations of the Table Mountain Latite rock
174 standard that yielded (^{234}U/^{238}U), (^{230}Th/^{238}U) and (^{226}Ra/^{230}Th) ratios that are within analytical
175 error of secular equilibrium (n = 6).

176

177 **4. RESULTS**

178 The new U-series isotope results are presented in Table 1 with accompanying major element
179 data for reference in supplementary Table S1. (^{234}U/^{238}U) is a sensitive measure of seawater
180 contamination and has been widely used to screen for the effects of alteration on U-series
181 disequilibria in submarine samples. Even though more recent multi-collector, inductively-coupled

mass spectrometric data achieves better precision (~ ± 0.5 %) than the TIMS data presented here (~ ± 1 %) all of the samples analysed here have ($^{234}U/^{238}U$) ratios within error of secular equilibrium and so we conclude that they are most likely relatively free from seawater alteration. 10 samples, were not successfully analysed for ($^{234}U/^{238}U$) and so the U-Th data for these must be treated with some caution. However, applying more zealous screening (e.g. on the basis of Cl/K ratios) does not change the primary observations from the data or the trends that are discussed below.

The SMAR U-Th isotope data span a significant range from secular equilibrium up to 32% ^{230}Th excess, similar to the full global range (Fig. 3A). With the exception of those sampled from segment A0, the basalts have quite high Th and U concentrations for MORB (up to 1.68 and 0.49 ppm, respectively; see Table 1), reflecting their overall trace element-enriched character. They have Th/U ratios of 3.0 to 3.5 that are similar to other MORB from slow-spreading sections of the Mid-Atlantic Ridge (e.g. Bourdon et al., 1996b; Lundstrom et al., 1998) but are distinctly higher than Th/U ratios from the fast-spreading East Pacific Rise (e.g. Lundstrom et al., 1999; Sims et al., 2002).

The average ($^{230}Th/^{238}U$) ratios increase from 1.10 in segment A0, to 1.13 in segment 4, to 1.14 in segment A3 to 1.19 in segment A2 to 1.32 in segment A1. Thus, there is no systematic north to south variation along the ridge. For the most part, the data from each ridge segment form a cluster on the equiline diagram (see Fig. 3A), though for each segment there are also some samples that plot away from the main group for that segment and overlap those from other segments. Note that these are not samples from the segment terminations, nor do they necessarily overlap the data from the adjacent segment. The biggest overlap occurs between the segments A0 and A2 and the greatest variation is observed along segment A2 (see Fig. 3A). Neither harsher screening on the basis of ($^{234}U/^{238}U$) ratios nor Cl/K ratios changes this observation.

^{226}Ra concentrations (2-215 fg/g) were determined on 55 of the samples. The majority of these have ^{226}Ra excesses beyond analytical accuracy (3 %). Because the age of the samples is unknown, the ^{226}Ra disequilibria must be considered as minima but do confirm that, for these

samples at least, no age correction need be applied to the U-Th disequilibria described above. For example, sample M41/2 202 DS-1 that is in U-Th equilibrium has 33% ^{226}Ra excess and many of the samples from segment A2 with high (^{230}Th/^{238}U) ratios also have ^{226}Ra excesses.

On a plot of (^{226}Ra/^{230}Th) versus (^{230}Th/^{238}U) some of the basalts from the A2 segment form a negative trend sub-parallel to that found in MORB from along the East Pacific Rise (see Fig. 3B) that formed the basis for the development of two-porosity, melt extraction models (Jull et al., 2002). The basalts that lie within error of ^{226}Ra-^{230}Th equilibrium most likely reflect decay of ^{226}Ra such that these samples can be estimated to be a millennia or so in age (see Fig. 3B). Restricting the remaining diagrams to only those samples with demonstrable ^{226}Ra excesses does not alter the results below because there are samples with ^{226}Ra excesses at both the low and high (^{230}Th/^{238}U) ends of the arrays discussed.

Finally, a recent study by O'Neill and Jenner (2013) raised the possibility that U-series disequilibria may become significantly modified by fractionation, tapping and replenishment processes occurring within the crust. However, we found no evidence for a correlation between either (^{230}Th/^{238}U) or (^{226}Ra/^{230}Th) and SiO_2 content (Fig. 4) from which we infer that the time scales for magma differentiation were less than the half-lives of the nuclides concerned (75 kyr and 1600 yr, respectively). Beier et al. (2015) reached a similar conclusion in their study of evolved magmas from the southeast rift in the Manus Basin and we assume for the purposes of following discussion that the variations in (^{230}Th/^{238}U) primarily reflect melting processes and/or source composition.

5. DISCUSSION

As shown by McKenzie (1985), the key parameters for creating U-series disequilibria by decompression melting of the mantle are the mineral-melt partition coefficients (D), the residual porosity of the melting region (ϕ), the length of the melt column and the melting rate Γ (in kg/m^3/s). In the case of MORB, the latter is linked to the upwelling rate W_s (in m/s) that will, in turn, equate

to the half-spreading rate of the ridge axis such that:

$$\Gamma = \rho_s^2 \, g \, W_s \, (\frac{dF}{dP}) \quad (1)$$

where ρ_s is the density of the solid (3300 kg/m^3), g is the acceleration due to gravity and dF/dP is the melt productivity due to decompression (in % melt/GPa). Richardson and McKenzie (1994) showed that an approximation of the disequilibria between a parent (p) and daughter (d) nuclide arising from melting in a 1D model can then be written as:

$$\left(\frac{d}{p}\right) = \frac{\lambda d \, (Dp + \phi) + \Gamma}{\lambda d \, (Dd + \phi) + \Gamma} \quad (2)$$

where λ is the decay constant of the relevant nuclide.

Due to the highly incompatible nature of Ra in mantle minerals (Blundy and Wood, 2003), ^{226}Ra-^{230}Th disequilibria is most sensitive to the porosity and so the presence of significant ^{226}Ra excesses in most of the SMAR basalts suggests that residual porosities were of the order of a few ‰ and we adopt a uniform value of 1 ‰ in all of the models discussed below. Under these conditions, ^{238}U-^{230}Th disequilibria is largely governed by the melting rate and partition coefficients. Thus, the slow spreading rate of the SMAR predicts low upwelling and melting rates that should, for a given peridotite composition, lead to large ^{230}Th excesses. Whilst this is indeed the case for some of the basalts (e.g. those from segments A1 and A2) our dataset encompasses almost the full range in ^{230}Th excess observed along mid-ocean ridges (Fig. 3A). Therefore, additional factors must have contributed to the range in U-Th disequilibria. In the following discussion we begin by assessing the evidence for control by variations in melt column length. Subsequently we explore the evidence for a potential role of source heterogeneities such as water, variable oxygen fugacity and the presence of recycled mafic lithologies followed by some quantitative numerical models.

5.1. Melt column length

As noted in the introduction, the 5-11°S section of the SMAR encompasses much of the global range in ridge depth and models in which the extent of ^{230}Th excess is largely controlled by

the depth to which the melt column penetrates down into the garnet stability zone predict a negative correlation between ^{230}Th excess and ridge depth (e.g. Bourdon et al., 1996a). High-pressure clinopyroxene can also retain U relative to Th but has less leverage than garnet such that magnitude of the resultant ^{230}Th excesses is smaller (Wood et al., 1999; Turner et al., 2000). On Fig. 5A we show the north to south variation in (^{230}Th/^{238}U) ratios as well as the variation in ridge depth. As can be seen there is little correspondence and overall an anti-correlation. This is emphasised on Fig. 5B which is a plot of (^{230}Th/^{238}U) versus ridge depth showing the results from the SMAR basalts as well as the very broad negative array formed by global, on-axis MORB data from the literature. The most striking thing is that the SMAR data do not follow the global trend and, if anything, they form an overall positive array. This result holds even if the samples not analysed for ^{226}Ra and any within analytical error of ^{226}Ra-^{230}Th secular equilibrium are omitted.

In detail, the majority of the basalts from segments A0 and A2-4 more or less overlap the global array although, taken together, these samples do not form a negative array either (see Fig. 5). However, the basalts from segment A1 lie well above global data from similarly deep ridge segments elsewhere. Deep ridges (i.e. thin crust) are inferred to be the product of relatively short melt columns in regions of lower than average mantle potential temperature (Klein and Langmuir, 1987). Irrespective of mantle lithology, such melting regimes should result in small ^{230}Th excesses (cf. Bourdon et al., 1996a; Elkins et al., 2014) yet this is clearly not the case for the basalts from segment A1. Moreover, basalts sampled at similar depths from segments A0 and A4 have markedly lower ^{230}Th excesses in comparison. It seems clear that, at least in the case of the SMAR, simple variations in melt column length cannot explain the range in U-Th disequilibria and a similar observation has been made for basalts from the South East Indian Ridge (Russo et al., 2009). In their recent study of the Artic Ridges, Elkins et al. (2014) concluded that variations in melt column length alone were insufficient to explain the observed U-series disequilibria and consequently appealed, in addition, to variations in source lithology.

285 *5.2. Variable H_2O or oxygen fugacity*

286 The simplest form of heterogeneity that can have a dramatic effect on U-Th disequilibria is
287 the presence of H_2O. As discussed by Bourdon et al. (2006), the presence of H_2O will promote a
288 deepening of the onset of partial melting thereby increasing the depth of penetration of the melt
289 column into the garnet stability field. This will result in increased ^{230}Th excess and that effect will
290 be enhanced further by the lower melt productivity of hydrous peridotite at the onset of melting
291 (e.g. Hirschmann et al., 1999; Asimow et al., 2004). Consistent with observations from MORB in
292 other plume-affected areas such as the mid-Atlantic Ridge across the Azores platform (Dixon et al.,
293 2002), the H_2O contents of the SMAR EMORB (segment A3) are higher than those of the NMORB
294 (segments A1 and A2). (Almeev et al., 2008). However, the observation that the ^{230}Th excesses are
295 higher in the basalts from segments A1 and A2 than those from segment A3 (Fig. 3A) is the exact
296 opposite of that anticipated from the effects of the presence of H_2O.

297 A possible mitigating factor to the reasoning just outlined is variation in the oxidation state
298 of the source region(s). The compatibility of U decreases markedly in mantle phases as the
299 oxidation state increases from QFM-1 to QFM or QFM+1 (e.g. Lundstrom et al., 1994). Thus, if the
300 more H_2O-rich sources of the EMORB are also more oxidised, this might act to significantly offset
301 or even overprint the effects of slower melting and a deeper melt column. However, EMORB from
302 segment A3 have equivalent or greater ^{230}Th excess to NMORB from segment A0 and we do not
303 observe any ^{238}U excesses in the SMAR dataset (cf. Beier et al., 2010). Moreover, we do not find
304 significant or correlated variations between (^{230}Th/^{238}U) and ratios like V/Sc (Fig. 6) that might
305 betray variations in oxygen fugacity (Mallmann and O'Neill, 2009). Thus, it seems unlikely that
306 oxidation state exerts a major control on U-Th disequilibria in the SMAR basalts.

307

308 *5.3. Recycled mafic lithologies*

309 As discussed at length by Hoernle et al. (2011), there is abundant trace element and
310 radiogenic isotope evidence for heterogeneity in the source regions of the SMAR basalts and we

explore this further on Fig. 7. Chondrite-normalised La/Sm_N ratios increase as εNd values decrease from those recording a long, time-integrated history of depletion (εNd ~ 13) to more enriched (εNd ~ 7) values characteristic of the EMORB basalts from segment A4 (Fig. 7A). As shown on Fig. 7B, this increase in La/Sm_N is accompanied by increasing Th/U ratios and the basalts from segment A1 appear to form their own array displaced to slightly lower La/Sm_N than the basalts from the other segments. Most notably, the basalts appear to separate into two parallel, positively sloped sub-trends on a plot of ($^{230}Th/^{238}U$) versus Th/U. The distinction between these two arrays is also geographic in its nature in as much as the basalts from segments A0-A2 in the north form one trend whilst those from segments A3 and A4 in the south form a second trend displaced to higher Th/U ratios (Fig. 7C). Note that, as might be anticipated from the geometry of the multiple component mixing relationships on Fig. 2B, there are no convincing correlations between ($^{230}Th/^{238}U$) and radiogenic isotope ratios such as $^{208}Pb/^{206}Pb$, either between or within the basalts from the different ridge segments (Fig. 8).

Similar correlations to those on Fig. 7C have been observed for some MORB before and attributed to mixing between melts formed under differing conditions (e.g. Lundstrom et al., 1998; Tepley et al., 2004). For example, Lundstrom et al. (1998) found such a trend in basalts from the north Mid-Atlantic Ridge and suggested that the low ($^{230}Th/^{238}U$), low Th/U end of their data reflected a melt near ^{238}U-^{230}Th equilibrium, either due to aging, or melting of a strongly depleted (e.g. near harzburgitic) source in which U and Th are not strongly fractionated. In the case of the SMAR basalts this is unlikely to be the case since many of the basalts at the low ($^{230}Th/^{238}U$) end of both of the arrays retain significant ^{226}Ra-^{230}Th disequilibrium and have elevated La/Sm_N ratios (cf. Fig. 7) that would be unlikely to result from melting of harzburgite.

Elkins et al. (2011, 2014) and Russo et al. (2009) have suggested that U-series disequilibria in many MORB reflect, at least in part, mixing of a peridotite melt with a melt from a recycled mafic lithology. This is an appealing option in the case of the SMAR given the trace element and radiogenic isotope evidence for the involvement of melts from an enriched component (cf. Figs. 2b,

7). Due to their higher melt productivity (Pertermann et al., 2003b, 2004), recycled mafic lithologies can lead to lower ($^{230}Th/^{238}U$) ratios than peridotite for a given upwelling rate (e.g. Stracke et al., 1999). However, the opposite is observed in the SMAR data whereby the basalts carrying an enriched signature (low εNd and elevated La/Sm_N and Th/U ratios) are those exhibiting the largest disequilibria (Fig. 7C). This suggests, at least in the case of the SMAR, that the effects of higher melt productivity may have been offset by the high proportions of garnet and high-pressure clinopyroxene that are present in recycled mafic lithologies.

5.4. Quantitative numerical models

On Fig. 9 we appraise a number of different, plausible models for the origin of the U-series disequilibria in the SMAR basalts on plots of ($^{230}Th/^{238}U$) versus Th/U, where the latter ratio is used as an index of relative source enrichment (cf. Fig. 7). We used the incremental dynamic melting model of Stracke et al. (2003) along with partition coefficients and source mineral modes listed in Table 2. For the MORB source we used the DMM composition (U = 0.0022 ppm, Th = 0.006 ppm) from Salters and Stracke (2004) and for the recycled mafic lithology for which we used an enriched composition (U = 0.102 ppm, Th = 0.405 ppm) with a Th/U ratio similar to many HIMU basalts (Sun and McDonough, 1989). We also assumed that the recycled mafic lithology begins to melt at 125 km, garnet peridotite at 100 km and that the garnet to spinel transition occurs at 75 km depth. The solid upwelling rate was set at the half spreading rate (0.016 m/yr) and the melt ascent rate was chosen to be 10 m/yr consistent with growing evidence that melt extraction occurs in channels (Turner et al., 2001; Stracke et al., 2006; Turner and Bourdon, 2010). As noted earlier, we assumed a porosity of 1 ‰ in all of the models.

On Fig. 9A we show the effect of changing bulk D's as a peridotite melting column penetrates down into the garnet stability zone. For a peridotite melt productivity of 15 %/GPa (Hirschmann et al., 1999) and an upwelling rate of 0.016 m/yr, equation 1 gives a melting rate, $\Gamma = 7.9 \times 10^{-5}$ kg/m^3/yr. Under these conditions and using bulk partition coefficients calculated from

Table 2, spinel peridotite produces an accumulated 10% melt with a slight ^{230}Th deficit whereas 10% melting of garnet peridotite yields a (^{230}Th/^{238}U) ratio of 1.25. In dynamic melting models, the Th/U ratio of the melt converges on that of the source once the accumulated extent of melting exceeds 1% (Elliot, 1997). MORB melts are likely to represent ~ 10% partial melts and so the change from melting in the spinel to garnet facies simply results in a vertical shift on Fig. 9A. The corollary is that no correlation is anticipated between (^{230}Th/^{238}U) and Th/U for a single source composition. Consequently, we explore more complex scenarios that include mixing between melts derived from sources with variable Th/U ratios.

Assuming the melt productivity of a recycled mafic lithology is closer to 30 %/GPa (Perterman and Hirschmann, 2003b) an upwelling rate of 0.016 m/yr corresponds to a melting rate, $\Gamma = 1.6 \times 10^{-4}$ kg/m^3/yr, significantly faster that that calculated for peridotite. This component could be either an eclogite or a garnet pyroxenite and these lithologies have different partition coefficients (see Table 2). For the chosen HIMU composition (see above), 12% melting this rate yields (^{230}Th/^{238}U) ratios of 1.56 and 1.30 for eclogite and pyroxenite, respectively. Because of the high Th/U ratio of this component, these compositions lie on the right hand side of Fig. 9A. As can be seen mixing between the eclogite and garnet peridotite melts cannot replicate the low (^{230}Th/^{238}U) ratios of many of the basalts from segments A2 and A4. Rather, the low (^{230}Th/^{238}U) ratios of these basalts (a number of which have resolvable ^{226}Ra excesses) seem to require a significant contribution of melt from spinel peridotite. Then, as shown on Fig. 9A, a mixing line between spinel peridotite and eclogite melts can simulate the compositions of many of the basalts from segments A0 to A2 whilst mixing of spinel peridotite and pyroxenite melts can reproduce those from segments A3 and A4. Such models are certainly consistent with the trace element and radiogenic isotope evidence for involvement of a recycled mafic lithology.

There are two other possible explanations for the origin of the separate arrays formed by the basalts. Because the amount of disequilibria is strongly dependent on the melting rate (cf. equations 1 and 2) even a modestly higher melting rate for the eclogite component will result in melt

compositions with significantly lower ($^{230}Th/^{238}U$) ratios (cf. Stracke et al., 1999). Such a change might reflect differences in the composition of the eclogite and/or its volatile content (cf. Fig. 2B) but we assume that, since the spreading rate does not change from north to south along this section of the SMAR, the melting rate of the peridotite component will remain constant. As shown on Fig. 9B, a small change in the melting rate of the eclogitic component (from $\Gamma = 1.6 \times 10^{-4}$ to 4.2×10^{-4} $kg/m^3/yr$) beneath the southern SMAR segments A3 and A4 could readily produce a shallower array that passes through these basalts. Although not shown to retain clarity, allowing two different melting rates for the pyroxenite could, in an analogous fashion, lead to two mixing lines that would simulate the two arrays formed by the SMAR basalts. However, an alternative solution to explain the two basalt arrays is that both the melting rates of both the peridotite and the recycled mafic lithology are constant along the SMAR but that the Th/U ratio of the peridotite simply changes southwards from one similar to NMORB to one more akin to EMORB on passing from segments A0-A2 to segments A3 and A4. The model on Fig. 9C demonstrates the equal ability of this latter scenario to account for the two SMAR arrays.

Distinguishing the relative viability of the models on Fig. 9 is problematic not least because the correlations in the data are insufficient to distinguish whether the arrays are truly parallel, convergent or divergent (see Fig. 7C). However, we have no independent evidence for why the melting rate or lithology of the recycled mafic component should change southwards beneath the SMAR whereas there is very good evidence for the presence of more than one enriched component in the sources of these basalts on Fig. 2C (cf. Hoernle et al., 2011). Thus, our preferred model is the one illustrated on Fig. 9C, and it is interesting that this calls for a southward change in composition of the peridotite end-member that does not translate to any change in melting dynamics as inferred from the range and extent of ^{230}Th excess. The implication is that the trace element and radiogenic isotope variations were imposed upon the source region(s) without any concomitant modification of mineralogy (and thus melting rate). One way in which this decoupling might be achieved is the model proposed by Prytulak and Elliott (2009) in which small degree melts from recycled mafic

lithologies infiltrate and freeze within overlying peridotite > 350 kyr prior to melting beneath the ridge axis. Any U-series disequilibria that might have existed in these melts will have decayed away such that their trace element and radiogenic isotope flavors are imparted on the infiltrated peridotite without significantly changing its modal mineralogy. In this way, the separation of the basalts from the A0-2 and A3/4 segments into two distinct arrays would then simply be a reflection of different source Th/U ratios.

It must be stressed that the many input parameters and assumptions required render the models shown on Fig. 9 plausible but non-unique. For example, we did not vary the melt column length other than the inception of melting for each of the different lithologies. This is a clear over simplification given the large variations in ridge depth but the lack of correlation with (^{230}Th/^{238}U) on Fig. 5A precludes doing this in any simple manner. Irrespective of these issues, all of the models require involvement of a recycled mafic lithology and the models on Fig. 9 suggest that the relative contributions from this component are small and between 2 and 4 % for the input compositions chosen. As noted by others, this does not need to imply this amount of recycled material in the mantle beneath the SMAR because such lithologies melt preferentially relative to peridotite.

6. CONCLUSIONS

It seems likely that there is a complex interplay of factors responsible for the pattern of U-Th disequilibria observed in the SMAR basalts. Conversely, because of the large number of parameters involved in disequilibria melting models, there will also be a range of subtly different models that can simulate the data in addition to the few end-member models that we have explored above. Nevertheless, we believe that there are several robust observations from the SMAR data that appear to differ from those obtained in some other recent studies:

1. the SMAR basalts preserve a large range of ^{230}Th excesses and these differ from segment to segment;

2. the ^{230}Th excesses are not negatively correlated with axial depth; the largest ^{230}Th excesses come from the deepest segment (A1);
3. the source regions of the SMAR basalts are demonstrably heterogeneous although there is only very broad correlations between ^{230}Th excesses and radiogenic isotope ratios;
4. two parallel and positively sloped correlations between ^{230}Th excesses and Th/U ratios can be explained by simple mixing between melts from spinel peridotite and a recycled mafic lithology;
5. if the increase in Th/U ratio between the two basalt arrays reflects mantle metasomatism this must have occured > 350 kyr prior to melting beneath the SMAR.

ACKNOWLEDGEMENTS

We gratefully acknowledge the professional support by the captains and crews of RV Meteor during cruises M41/2, M64/1 and M68/1. The research presented here was funded by the Deutsche Forschungsgemeinschaft (DFG) under grants HA 2568/14-1 and -2 to K. Haase and F. Hauff as part of the DFG Priority Program SPP 1144 “From Mantle to Ocean”. The manuscript was written in Kiel during the summer of 2014 whilst S.T. was the very grateful recipient of a Humboldt Research Award. The comments of two anonymous reviewers and associate editor Tony Dosseto helped to improve the manuscript.

462 **REFERENCES**

463 Almeev R., Holtz F., Koepke J., Haase K. and Devey C. (2008) Depths of partial crystallization of
464 H_2O-bearing MORB: Phase equilibria simulations of basalts at the MAR near Ascension
465 Island (7-11ºS). *J. Petrol.* **49**, 25-45.
466 Asimow P. D., Dixon J. E. and Langmuir, C. H. (2004) A hydrous melting and fractionation model
467 for mid-ocean ridge basalts: application to the Mid-Atlantic Ridge near the Azores. *Geochem.*
468 *Geophys. Geosys.* **5**, doi:10.1029/2003GC000568.
469 Beattie P. (1993) Uranium thorium disequilibria and partitioning on melting of garnet peridotite.
470 *Nature* **363**, 63–65.
471 Beier C., Turner S. P., Sinton J. M. and Gill J. B. (2010) Influence of subducted components on
472 back-arc melting dynamics in the Manus Basin. *Geochem. Geophys. Geosys.* **5**, Q0AC03.
473 Beier C., Bach W., Turner S., Niedermeier D., Woodhead J., Erzinger J. and Krumm S. (2015).
474 Origin of silicic magmas at spreading centres – an example from the South East Rift, Manus
475 Basin. *J. Petrol.* **56**, 255-272.
476 Blundy J. D. and Wood B. J. (2003) Mineral-melt partitioning of uranium, thorium, and their
477 daughters. *Rev. Mineral. Geochem.* **52**, 59–123.
478 Bourdon B., Zindler A., Elliott T. and Langmuir C. H. (1996a) Constraints on mantle melting at
479 mid-ocean ridges from global U-238-Th-230 disequilibrium data. *Nature* **384**, 231–235.
480 Bourdon B., Langmuir C. H. and Zindler A. (1996b) Ridge-hotspot interaction along the Mid-
481 Atlantic Ridge between 37 degrees 30’ and 40 degrees 30’N: the U–Th disequilibrium
482 evidence. *Earth Planet. Sci. Lett*. **142**, 175–189.
483 Bourdon B., Turner S. P. and Ribe N. M. (2005) Partial melting and upwelling rates beneath the
484 Azores from a U-series isotope perspective. *Earth Planet. Sci. Lett.* **239**, 42–56.
485 Brozena J. M. (1986) Temporal and spatial variability of seafloor spreading processes in the
486 Northern South Atlantic. *J. Geophys. Res.* **91**, 497–510.
487 Bruguier N. J., Minshull T. A. and Brozena J. M. (2003) Morphology and tectonics of the Mid-

Atlantic Ridge, 7°–12°S. *J. Geophys. Res.* **108**, doi:10.1029/2001JB001172.

DeMets C., Gordon R. G., Argus D. F. and Stein S. (1994) Effect of recent revisions to the geomagnetic reversal timescale on estimates of current plate motions. *Geophys. Res. Lett.* **21**, 2191–2194.

Dixon J. E., Leist L., Langmuir C. H. and Schilling J.-G. (2002) Recycled dehydrated lithosphere observed in plume-influenced mid-ocean ridge basalt. *Nature* **420**, 385-389.

Eiler J. M. (2000) Oxygen isotope variations of basaltic lavas and upper mantle rocks. *Rev. Mineral. Geochem.* **43**, 319-364.

Elkins L. J., Sims K. W. W., Prytulak J., Mattielli N., Elliott T., Blichert-Toft J., Blusztajn J., Dunbar N., Devey C. W. Mertz, D. F. and Schilling J. G. (2011) Understanding melt generation beneath the slow spreading Kolbeinsey Ridge from ^{238}U, ^{230}Th, and ^{231}Pa excesses. *Geochim. Cosmochim. Acta* **75**, 6300–6329.

Elkins L. J., Sims K. W. W., Prytulak J., Blichert-Toft J., Elliott T., Blusztajn J., Fretzdorff S., Reagan M., Hasse K., Humphris S. and Schilling J.G. (2014) Melt generation beneath Arctic Ridges: Implications from U decay series disequilibria in the Mohns, Knipovich, and Gakkel Ridges. *Geochim. Cosmochim. Acta* **127**, 140-170.

Elliott T. (1997) Fractionation of U and Th during mantle melting: a reprise. *Chem. Geol.* **139**, 165-183.

Elliott T. and Spiegelman M. (2003) Melt migration in oceanic crustal production: A U-series perspective. In *Treatise on Geochemistry* (ed. R.L. Rudnick). Elsevier, Amsterdam, pp. 465–510.

Hirschmann M. M. and Stolper E. M. (1996) A possible role for garnet pyroxenite in the origin of the garnet signature in MORB. *Contrib. Mineral. Petrol.* **124**, 185–208.

Hirschmann M. M., Asimow P. D., Ghiorso M. S. and Stolper E. M. (1999) Calculation of peridotite partial melting from thermodynamic models of minerals and melts. III. Controls on isobaric melt production and the effect of water on melt production. *J. Petrol.* **40**, 831-851.

514 Hoernle K., Hauff F., Kokfelt T. F., Hasse K., Garbe-Schonberg D. and Werner R. (2011) On- and
515 off-axis chemical heterogeneities along the South Atlantic Mid-Ocean-Ridge (5-11°S):
516 Shallow or deep recycling of ocean crust and/or intraplate volcanism? *Earth Planet. Sci. Lett.*
517 **306**, 86-97.
518 Iwamori H. (1994) ^{238}U–^{230}Th–^{226}Ra- and ^{235}U–^{231}Pa disequilibria produced by mantle melting with
519 porous and channel flows. *Earth Planet. Sci. Lett.* **125**, 1–16.
520 Jarosewich E. J., Nelen J. A and Norberg J. A. (1980) Reference samples for electron microprobe
521 analysis. *Geostand. Newslett.* **4**, 43-47.
522 Klein E. M. and Langmuir C. H. (1987) Global correlations of ocean Ridge Basalt chemistry with
523 axial depth and crustal thickness. *J. Geophys. Res.* **92**, 8089–8115.
524 Kogiso T., Hirschmann M. M. and Pertermann M. (2004) High-pressure partial melting of mafic
525 lithologies in the mantle. *J. Petrol.* **45**, 2407–2422.
526 Kokfelt T. F., Lundstrom C., Hoernle K., Hauff F., Fiebig J. and Werner R. (2005) Plume-ridge
527 interaction studies at the Galapagos spreading center: evidence from ^{226}Ra-^{230}Th-^{238}U and
528 ^{231}Pa-^{235}U isotopic disequilibria. *Earth Planet. Sci. Lett.* **234**, 165-187.
529 Jull M., Kelemen P. B. and Sims K. W. W. (2002) Consequences of diffuse and channeled porous
530 melt migration on uranium series disequilibria. *Geochim. Cosmochim. Acta* **66**, 4133–4148.
531 Lundstrom C. C., Shaw H. F., Ryerson F. J., Phinney D. L., Gill J. B. and Williams Q. (1994)
532 Compositional controls on the partitioning of U, Th, Ba, Pb, Sr and Zr between clinopyroxene
533 and haplobasaltic melts: Implications for uranium series disequilibria in basalts. *Earth Planet.*
534 *Sci. Lett.* **128**, 407–423,
535 Lundstrom C. C., Gill J., Williams Q. and Hanan B. B. (1998) Investigating solid mantle upwelling
536 beneath mid-ocean ridges using U-series disequilibria. II. A local study at 33°S Mid-Atlantic
537 Ridge. *Earth Planet. Sci. Lett.* **157**, 167-181.
538 Lundstrom C. C., Sampson D. E., Perfit M. R., Gill J. and Williams Q. (1999) Insights into mid-
539 ocean ridge basalt petrogenesis: U-series disequilibria from the Siqueiros transform, Lamont

Seamounts and East Pacific Rise. *J. Geophys. Res.* **104**, 13035–13048.

Mallmann G. and O'Neill H. St. C. (2009) The crystal/melt partitioning of V during mantle melting as a function of oxygen fugacity compared with some other elements (Al, P, Ca, Sc, Ti, Cr, Fe, Ga, Y, Zr and Nb). *J. Petrol.* **50**, 1765-1794.

Mckenzie D. (1985) Th-230–U-238 disequilibrium and the melting processes beneath ridge axes. *Earth Planet. Sci. Lett.* **72**, 149–157.

Minshull T. A., Bruguier N. J. and Brozena J. M. (1998) Ridge–plume interactions or mantle heterogeneity near Ascension Island? *Geology* **26**, 115–118.

O'Neill H. St. C. and Jenner F. E. (2013) The global pattern of trace-element distributions in ocean floor basalts. *Nature* **491**, 698-704.

Paulick H., Munker C. and Schuth S. (2010) The influence of small-scale mantle heterogeneities on Mid-Ocean Ridge volcanism: Evidence from the southern Mid-Atlantic Ridge (7º30'S to 11º30'S) and Ascension Island. *Earth Planet. Sci. Lett.* **296**, 299-310.

Peate D. W., Hawkesworth C. J., van Calsteren P. W., Taylor R. N. and Murton B. J. (2001) U-238–Th-230 constraints on mantle upwelling and plume-ridge interaction along the Reykjanes Ridge. *Earth Planet. Sci. Lett.* **187**, 259–272.

Pertermann M. and Hirschmann M. (2003a) Partial melting experiments on MORB-like pyroxenite between 2 and 3 GPa: Constraints on the presence of pyroxenite in basalt source regions from solidus location and melting rate. *J. Geophys. Res.* **108**, 2125.

Pertermann M. and Hirschmann M. (2003b) Anhydrous partial melting experiments on MORB-like eclogite: phase relations, phase compositions and mineral-melt partitioning of major elements at 2–3 GPa. *J. Petrol.* **44**, 2173–2201.

Pertermann M., Hirschmann M. M., Hametner K., Gunther D. and Schmidt M. W. (2004) Experimental determination of trace element partitioning between garnet and silica-rich liquid during anhydrous partial melting of MORB-like eclogite. *Geochem. Geophys. Geosyst.* **5**, Q05A01.

566 Prytulak J. and Elliott T. (2009) Determining melt productivity of mantle sources from U-238–Th-
567 230 and U-235–Pa-231 disequilibria; an example from Pico Island Azores. *Geochim.*
568 *Cosmochim. Acta* **73**, 2103–2122.
569 Richardson C. and McKenzie D (1994) Radioactive disequilibria from 2D models of melt
570 generation by plumes and ridges. *Earth Planet. Sci. Lett.* **128**, 425-437.
571 Russo C. J., Rubin K. H. and Graham D. W. (2009) Mantle melting and magma supply to the
572 Southeast Indian Ridge: the roles of lithology and melting conditions from U-series
573 disequilibria. *Earth Planet. Sci. Lett.* **278**, 55–66.
574 Ryan W. B. F., Carbotte S. M., Coplan J. O., O'Hara S., Melkonian A., Arko R., Weissel R. A.,
575 Ferrini V., Goodwillie A., Nitsche F., Bonczkowski J., Zemsky R. (2009) Global multi-
576 resolution topography synthesis. *Geochem. Geophys. Geosyst.* **10**, Q03014.
577 Salters V. J. M., Longhi J. E. and Bizimis M. (2002) Near mantle solidus trace element partitioning
578 at pressures up to 3.4 GPa. *Geochem. Geophys. Geosyst.* **3**, Q1038.
579 Salters V. J. M. and Stracke A. (2004) Composition of the depleted mantle. *Geochem. Geophys.*
580 *Geosyst.* **5**, 000013.
581 Sims K. W. W., Goldstein S. J., Blichert-Toft J., Perfit M. R., Kelemen P., Fornari D. J., Michael
582 P., Murrell M. T., Hart S. R., DePaolo D. J., Layne G., Ball L., Jull M. and Bender J. (2002).
583 Chemical and isotopic constraints on the generation and transport of magma beneath the East
584 Pacific Rise. *Geochim. Cosmochim. Acta* **66**, 3481–3504.
585 Stracke A., Salters V. J. M. and Sims K. W. W. (1999) Assessing the presence of garnet-pyroxenite
586 in the mantle sources of basalts through combined hafnium-neodymium-thoruim isotope
587 systematics. *Geochem. Geophys. Geosyst.* **3**, Q05004.
588 Stracke A., Zindler A., Salters V. J. M., McKenzie D. and Gronvold K. (2003) The dynamics of
589 melting beneath Theistareykir, northern Iceland. *Geochem. Geophys. Geosyst.* **4**, 8513.
590 Stracke A., Bourdon B. and McKenzie D. (2006) Melt extraction in the Earth's mantle: constraints
591 from U–Th–Pa–Ra studies in oceanic basalts. *Earth Planet. Sci. Lett.* **244**, 97–112.

592 Sun S.-S. and McDonough W. F. (1989) Chemical and isotopic systematics of oceanic basalts:
593 implications for mantle composition and processes. *Geol. Soc. Lond. Spec. Publ.* **42**, 313-345.
594 Tepley F.J ., Lundstrom C. C., Sims K. W. W. and Hekinian R. (2004) U-series disequilibria in
595 MORB from the Garrett transform and implications formantlemelting. *Earth Planet. Sci. Lett.*
596 **223**, 79–97.
597 Turner S., Blundy J., Wood B. and Hole M. (2000) Large ^{230}Th-excesses in basalts produced by
598 partial melting of spinel lherzolite. *Chem. Geol.* **162**, 127-136.
599 Turner S., Evans P. and Hawkesworth C. (2001) Ultra-fast source-to-surface movement of melt at
600 island arcs from ^{226}Ra-^{230}Th systematics. *Science* **292**, 1363-1366.
601 Turner S. and Bourdon B. (2010) Melt transport from the mantle to the crust – U-series isotopes. In,
602 Dosseto A., Turner S. and Van Orman J. (eds) *Timescales of magmatic processes: from core*
603 *to atmosphere.* Wiley-Blackwell, pp. 102-115.
604 Wanless V. D., Perfit M. R., Ridley W. I. and Klein E (2010) Dacite petrogenesis on mid-ocean
605 ridges: evidence for oceanic crustal melting and assimilation. *J. Petrol.* **51**, 2377-2410.
606 Waters C. L., Sims K. W. W., Perfit M. R., Blichert-Toft J. and Blusztajn J. (2011) Perspective on
607 the genesis of E-MORB from chemical and isotopic heterogeneity at 9_–10_N East Pacific
608 Rise. *J. Petrol.* **52**, 565–602.
609 Wood B. J., Blundy J. D. and Robinson J. A. C. (1999) The role of clinopyroxene in generating U-
610 series disequilibrium during mantle melting. *Geochim. Cosmochim. Acta* **63**, 1613-1620.
611

612 **Fig. 1.** (A) Overview bathymetric map showing the South Atlantic Mid-Ocean Ridge (SMAR) that
613 can be divided in four ridge segments going from A0 to the north of the Acension fracture zone and
614 through A1 to A4 to the south of the fracture zone. Also shown is Ascension Island located adjacent
615 to segment A1. The dredge locations for the studied samples are indicated by the filled red circles
616 with expanded maps of areas from which many samples were obtained from a relatively small area
617 with a ROV given in panels (B) and (C). Three geochemical domains were defined by Hoernle et al.
618 (2011): Ascension Island/A1 ridge segment (blue dashed line), the A2 ridge segment (yellow
619 dashed line), and the A3+A4 ridge segment (red dashed line) domains. The A1–A2 boundary is
620 presently propagating northwards (Brozena, 1986; Bruguier et al., 2003). The A2–A3 boundary is
621 interpreted to presently be an overlapping spreading center with left-lateral displacement, but was a
622 transform fault with right-lateral offset at the same location for at least 36 Ma before the A3 ridge
623 jump at ≥ 1 Ma ago (Brozena, 1986; Bruguier et al., 2003). The trace of the transform boundary is
624 denoted as Fracture Zone A (FZA) after Brozena (1986). Before the ridge jump the A3 and A4
625 segments were probably continuous (Bruguier et al., 2003). Map created using the
626 GeoMapApplication tool (http://www.geomapapp.org, Ryan et al., 2009).
627
628 **Fig. 2.** (A) Plot of K_2O/TiO_2 x 100 versus SiO_2 dividing the samples into NMORB and EMORB.
629 (B) Plot of $^{143}Nd/^{144}Nd$ versus $^{208}Pb/^{206}Pb$ showing the five spatial-geochemical subdivisions of the
630 data. As discussed in detail by Hoernle et al. (2011), these data seem to require the presence of at
631 least one depleted end-member, inferred to be depleted MORB mantle (DMM), but see also Paulick
632 et al. (2010), and three enriched end-members as indicated.
633
634 **Fig. 3.** (A) U-Th equiline plot showing that the SMAR basalts span a significant range in
635 disequilibria largely cluster into ridge segments though A0 overlaps with A2 and A3 with A4. (B)
636 Plot of ($^{226}Ra/^{230}Th$) versus ($^{230}Th/^{238}U$) showing that the SMAR basalts have both ^{226}Ra excesses
637 and deficits (especially those from segment A1). Many of the basalts from the A2 segment for a

negative trend sub-parallel to that found along the East Pacific Rise. Shown for comparison are global, on-axis MORB data (Bourdon et al., 1996a,b; Lundstrom et al., 1998; Peate et al., 2001; Sims et al., 2002; Kokfelt et al., 2005; Russo et al., 2009; Elkins et al., 2011, 2014). Grey, short-dashed lines on (A) indicate percentage ^{230}Th excess, black, long-dashed lines on (B) indicate secular equilibrium.

Fig. 4. Plot of (^{230}Th/^{238}U) versus SiO_2 showing that the extent of disequilibria is not linked to indices of differentiation, either within or between the different SMAR ridge segments.

Fig. 5. (A) Plot of (^{230}Th/^{238}U) versus latitude for SMAR basalts overlain upon ridge depth (dashed line). (B) Plot of (^{230}Th/^{238}U) versus ridge depth for SMAR basalts in comparison with the global, on-axis MORB dataset (Bourdon et al., 1996a,b; Lundstrom et al., 1998; Peate et al., 2001; Sims et al., 2002; Kokfelt et al., 2005; Russo et al., 2009; Elkins et al., 2011, 2014). Black dashed line indicates secular equilibrium.

Fig. 6. The lack of correlation between (^{230}Th/^{238}U) and V/Sc suggests that the extent of disequilibria is not linked to indices of oxygen fugacity in the mantle source regions (cf. Mallmann and O'Neill, 2009).

Fig. 7. Plots of (A) εNd versus chondrite-normalised La/Sm_N ratio, (B) Th/U versus La/Sm_N and (C) (^{230}Th/^{238}U) versus Th/U showing that the SMAR data require at least one depleted and one enriched end-member source composition (cf. Fig. 2B). On (B) the basalts from segment A1 form a separate trend parallel to the others basalts but displaced to lower La/Sm_N whilst on (C) there appears to be two groupings with sub-parallel, positive trends – one for the basalts from the northern segments A0-A2 and one for those from the southerly segments A3 and A4.

664 **Fig. 8.** Plot of (^{230}Th/^{238}U) versus ^{208}Pb/^{206}Pb showing that there is no clear correlation within or
665 between the different ridge segments.

666

667 **Fig. 9.** Comparison of the results of the numerical models that the SMAR basalts on plots of
668 (^{230}Th/^{238}U) versus Th/U. (A) Mixing between spinel and garnet peridotite melts ($\Gamma = 7.9 \times 10^{-5}$
669 kg/m^3/yr) and an eclogite or pyroxenite melt ($\Gamma = 1.6 \times 10^{-4}$ kg/m^3/yr). (B) Mixing between spinel-
670 peridotite melt and an eclogite melt formed at two differing rates of melting as indicated. (C)
671 Mixing between spinel peridotite melts from normal and enriched MORB source compositions and
672 a single eclogite melt for which $\Gamma = 1.6 \times 10^{-4}$ kg/m^3/yr. The proportions of eclogite added in the
673 mixing models are indicated along the curves in increments of 2 %. All models used the
674 incremental dynamic melting formulation of Stracke et al. (2003) and the mineral/melt partition
675 coefficients listed in Table 2. See text for other model inputs and further discussion.

676
677

Table 1. Uranium series and oxygen isotope data for South Mid-Atlantic Ridge basalts.

Sample #	Lat.	Long.	Depth (m)	U (µg/g)	Th (µg/g)	Th/U	± 2 s.e.	($^{234}U/^{238}U$)
Segment A0								
M41/2 119 DS-1	6.273	11.376	3242	0.043	0.127	2.923	0.007	1.006
M41/2 120 DS-2	6.399	11.338	3523	0.021	0.061	2.919	0.019	0.971
M41/2 121 DS-1	6.542	11.310	3749	0.066	0.204	3.102	0.015	1.004
M41/2 122 DS-5	6.664	11.293	4080	0.073	0.220	3.005	0.016	1.005
Segment AFZ								
M41/2 126 DS-1	7.138	13.050	4514	n.d.	0.035	n.d.	n.d.	n.d.
M41/2 126 DS-2	7.138	13.050	4514	0.011	0.035	3.172	0.018	n.d.
Segment A1								
M41/2 130 DS-1	7.584	13.470	3925	0.010	0.029	2.999	0.018	n.d.
M41/2 132 DS-1	7.666	13.456	3925	0.147	0.506	3.434	0.018	1.000
M41/2 133 DS-7	7.718	13.444	3980	0.092	0.302	3.290	0.015	0.993
M41/2 136 DS-1	7.773	13.432	3727	0.097	0.342	3.510	0.013	1.000
M41/2 137 DS-2	7.820	13.427	3405	0.060	0.206	3.412	0.018	1.007
M41/2 139 DS-3	7.919	13.411	3631	0.117	0.405	3.470	0.012	1.002
M41/2 140 DS-1	7.965	13.399	3670	0.052	0.173	3.343	0.016	0.998
M41/2 141 DS-1	7.986	13.431	3364	0.034	0.113	3.344	0.016	0.993
M41/2 142 DS-2	8.019	13.430	3576	0.086	0.297	3.439	0.013	1.000
M41/2 142 DS-3	8.019	13.430	3576	0.086	0.295	3.409	0.013	1.001
M41/2 143 DS-2	8.055	13.417	3457	0.024	0.077	3.167	0.017	n.d.
M41/2 143 DS-2*	8.055	13.417	3457	0.024	0.077	3.167	0.017	n.d.
M41/2 146 DS-2	8.167	13.446	3401	0.099	0.338	3.416	0.017	0.999
Segment A2								

M64/1 159ROV11	8.791	13.503	2219	0.131	0.422	3.234	0.013	0.993
M64/1 159ROV9	8.792	13.504	2215	0.125	0.407	3.250	0.014	1.013
M41/2 149 DS-2	8.374	13.616	3063	0.243	0.795	3.271	0.015	1.000
M64/1 159ROV7	8.796	13.504	2201	0.126	0.405	3.199	0.012	1.001
M64/1 159ROV8	8.796	13.504	2202	0.125	0.409	3.259	0.013	0.992
M64/1 159ROV10	8.791	13.503	2219	0.131	0.435	3.323	0.015	0.997
M64/1 155ROV-6	8.817	13.501	2190	0.161	0.525	3.261	0.014	1.004
M64/1 156VSR	8.807	13.507	2208	0.122	0.393	3.224	0.011	1.001
M41/2 162 DS-1	9.080	13.445	2460	0.138	0.427	3.090	0.018	n.d.
M41/2 162 DS-1	9.080	13.445	2460	0.138	0.427	3.090	0.018	n.d.
M41/2 158 DS-1	8.838	13.495	2139	0.154	0.493	3.202	0.010	1.000
M64/1 159ROV3	8.801	13.502	2198	0.124	0.403	3.259	0.015	1.007
M64/1 155ROV-3	8.817	13.505	2149	0.159	0.509	3.214	0.011	1.000
M64/1 159ROV1	8.803	13.502	2204	0.126	0.405	3.227	0.026	0.999
M41/2 153 DS-1	8.555	13.550	2552	0.144	0.469	3.266	0.014	1.005
M64/1 155ROV-5	8.817	13.501	2199	0.121	0.386	3.181	0.014	1.007
M64/1 159ROV4	8.800	13.502	2201	0.124	0.407	3.279	0.021	0.993
M64/1 155ROV-4	8.816	13.503	2195	0.121	0.390	3.224	0.011	0.998
M64/1 159ROV2	8.803	13.502	2201	0.125	0.405	3.228	0.012	1.006
M64/1 155ROV-7	8.817	13.500	2221	0.122	0.385	3.156	0.013	1.004
M64/1 159ROV5	8.799	13.503	2186	0.050	0.141	2.812	0.011	0.989
M64/1 155ROV-8	8.817	13.498	2218	0.117	0.369	3.146	0.014	1.000
M41/2 157 DS-3	8.808	13.496	2212	0.121	0.382	3.162	0.013	1.009
M64/1 163VSR	8.757	13.512	2287	0.121	0.381	3.152	0.016	0.991
M64/1 159ROV6	8.797	13.503	2151	0.047	0.140	2.951	0.013	1.003
M64/1 160VSR	8.782	13.507	2208	0.135	0.427	3.166	0.014	1.015
M64/1 162VSR	8.770	13.511	2273	0.075	0.239	3.175	0.012	1.000
M41/2 161 DS-1	9.013	13.457	2232	0.055	0.174	3.135	0.020	1.000
M64/1 155ROV-1	8.816	13.508	2161	0.036	0.103	2.887	0.017	1.019
M64/1 161VSR	8.778	13.510	2266	0.109	0.339	3.099	0.015	1.001
M41/2 160 DS-2	8.968	13.460	2166	0.033	0.097	2.917	0.015	1.009

Segment A3								
M41/2 166 DS-4	9.230	13.316	2299	0.335	1.142	3.412	0.013	1.000
M68/1 36VSR	9.532	13.213	1439	0.314	1.045	3.332	0.013	0.998
M64/1 203VSR	9.545	13.211	1509	0.348	1.203	3.456	0.016	1.001
M64/1 213GTV-1	9.547	13.209	1513	0.332	1.060	3.196	0.014	1.005
M64/1 214GTV-1	9.547	13.209	1511	0.327	1.032	3.153	0.014	1.005
M64/1 209GTV-1	9.548	13.209	1511	0.302	1.013	3.352	0.016	0.999
M64/1 200ROV-2	9.549	13.213	1523	0.451	1.509	3.349	0.012	0.994
M64/1 200ROV-3	9.548	13.212	1505	0.326	1.099	3.372	0.014	0.999
M64/1 200ROV-6	9.549	13.209	1496	0.358	1.189	3.325	0.010	1.005
M64/1 200ROV-12	9.545	13.209	1495	0.309	1.009	3.268	0.013	1.014
M68/1 33VSR	9.552	13.211	1479	0.364	1.220	3.347	0.016	1.000
M64/1 205VSR	9.558	13.209	1497	0.303	1.025	3.377	0.012	0.996
M41/2 172 DS-3	9.560	13.210	1488	0.321	1.086	3.381	0.009	0.999
M64/1 211VSR	9.569	13.209	1488	0.312	1.053	3.376	0.016	1.000
M64/1 194ROV-1	9.573	13.216	1454	0.390	1.298	3.329	0.013	1.001
M64/1 194ROV-4	9.573	13.214	1429	0.476	1.579	3.317	0.013	1.002
M64/1 194ROV-7	9.573	13.211	1448	0.308	1.037	3.370	0.013	1.002
M64/1 194ROV-9	9.574	13.209	1465	0.307	1.033	3.359	0.015	1.005
M64/1 194ROV-10	9.573	13.208	1470	0.294	1.018	3.456	0.013	1.011
M64/1 194ROV-11	9.573	13.208	1470	0.313	1.050	3.359	0.015	1.006
M64/1 194ROV-12	9.573	13.206	1460	0.306	1.012	3.305	0.009	0.999
M64/1 194ROV-13	9.573	13.206	1468	0.225	0.753	3.353	0.019	1.017
M41/2 174 DS-2	9.704	13.157	1539	0.492	1.648	3.350	0.009	1.003
M41/2 190 DS-2	9.887	13.087	2052	0.301	1.009	3.350	0.009	1.002
M41/2 190 DS-4	9.887	13.087	2052	0.207	0.679	3.282	0.016	0.995
Segment A4								
M41/2 194 DS-1	10.071	13.198	2953	0.115	0.374	3.263	0.017	1.002
M41/2 195 DS-2	10.132	13.197	3091	0.062	0.199	3.223	0.015	1.010
M41/2 196 DS-3	10.231	13.189	3241	0.246	0.818	3.317	0.011	0.999

M41/2 198 DS-1	10.382	13.178	3500	0.063	0.211	3.343	0.015	1.007
M41/2 199 DS-2	10.484	13.170	3528	0.032	0.103	3.202	0.017	n.d.
M41/2 200 DS-1	10.609	13.092	3791	0.096	0.310	3.250	0.013	1.005
M41/2 201 DS-5	10.684	13.075	3712	0.168	0.597	3.563	0.013	1.004
M41/2 202 DS-1	10.782	13.051	3463	0.022	0.066	3.012	0.013	n.d.
M41/2 203 DS-2	10.882	13.038	3639	0.057	0.176	3.087	0.022	1.030
TML (n=6)	-	-	-	10.690	29.740	2.782	0.028	1.008

Decay constants used: $\lambda^{226}Ra = 4.3322x10^{-4}$; $\lambda^{230}Th = 9.1577x10^{-6}$; $\lambda^{232}Th = 4.9475x10^{-11}$; $\lambda^{234}U = 2.8263x10^{-6}$; $\lambda^{238}U = 1.55125x10^{-10}$.

* Replicate Analyses of seperate digestions. Errors are 2s analytical internal errors. n.d. = not determined.

680
681

± 2 s.e.	(^{238}U/^{232}Th)	± 2 s.e.	(^{230}Th/^{232}Th)	± 2 s.e.	(^{230}Th/^{238}U)	± 2 s.e.	^{226}Ra (fg/g)	± 2 s.e.	(^{226}Ra/^{230}Th)	± 2 s.e.
0.005	1.038	0.002	1.184	0.014	1.140	0.014	22.7	0.4	1.356	0.029
0.020	1.040	0.007	1.168	0.005	1.124	0.009	n.d.	n.d.	n.d.	n.d.
0.010	0.978	0.005	1.130	0.026	1.155	0.027	30.3	0.5	1.180	0.034
0.008	1.010	0.005	1.154	0.009	1.143	0.011	27.1	0.5	0.961	0.018
n.d.	1.283	0.009	1.263	0.114	0.984	0.089	n.d.	n.d.	n.d.	n.d.
n.d.	0.957	0.005	n.d.	n.d.	n.d.	n.d.	2.84	0.05	2.636	0.177
	1.012	0.006	1.256	0.021	1.241	0.020	n.d.	n.d.	n.d.	n.d.
0.003	0.884	0.005	1.038	0.008	1.175	0.011	n.d.	n.d.	n.d.	n.d.
0.014	0.922	0.004	1.123	0.008	1.218	0.010	n.d.	n.d.	n.d.	n.d.
0.006	0.864	0.003	1.107	0.023	1.280	0.027	n.d.	n.d.	n.d.	n.d.
0.014	0.889	0.005	1.172	0.012	1.317	0.015	28.0	0.4	1.042	0.018
0.005	0.875	0.003	1.155	0.010	1.321	0.012	n.d.	n.d.	n.d.	n.d.
0.006	0.908	0.004	1.166	0.012	1.284	0.015	n.d.	n.d.	n.d.	n.d.
0.011	0.907	0.004	1.175	0.011	1.295	0.012	n.d.	n.d.	n.d.	n.d.
0.007	0.882	0.003	1.112	0.013	1.260	0.015	n.d.	n.d.	n.d.	n.d.
0.003	0.890	0.004	1.138	0.015	1.278	0.018	41.6	0.6	1.115	0.022
n.d.	0.958	0.005	1.150	0.012	1.200	0.014	17.0	0.1	1.675	0.029
n.d.	0.958	0.005	1.150	0.012	1.200	0.014	15.5	0.2	1.579	0.044
0.006	0.888	0.004	1.095	0.014	1.233	0.017	41.2	0.8	1.001	0.023

0.007	0.938	0.004	1.146	0.010	1.222	0.012	n.d.	n.d.	n.d.	n.d.
0.011	0.934	0.004	1.130	0.011	1.210	0.013	74.9	0.6	1.466	0.019
0.006	0.928	0.004	1.062	0.009	1.144	0.011	106.4	1.3	1.133	0.017
0.005	0.948	0.004	1.152	0.009	1.215	0.011	72.6	0.6	1.400	0.017
0.006	0.931	0.004	1.127	0.016	1.210	0.018	n.d.	n.d.	n.d.	n.d.
0.007	0.913	0.004	1.117	0.013	1.224	0.015	n.d.	n.d.	n.d.	n.d.
0.007	0.930	0.004	1.095	0.014	1.177	0.016	n.d.	n.d.	n.d.	n.d.
0.005	0.941	0.003	1.148	0.013	1.220	0.015	n.d.	n.d.	n.d.	n.d.
n.d.	0.982	0.006	1.127	0.011	1.148	0.013	57.2	0.7	1.068	0.016
n.d.	0.982	0.006	1.127	0.011	1.148	0.013	n.d.	n.d.	n.d.	n.d.
0.004	0.947	0.003	1.149	0.008	1.212	0.009	88.2	0.7	1.400	0.015
0.006	0.931	0.004	1.162	0.013	1.248	0.015	n.d.	n.d.	n.d.	n.d.
0.004	0.944	0.003	1.169	0.013	1.238	0.014	96.6	0.9	1.459	0.021
0.016	0.940	0.008	1.157	0.015	1.231	0.019	n.d.	n.d.	n.d.	n.d.
0.004	0.929	0.004	1.144	0.011	1.232	0.013	78.3	0.8	1.311	0.018
0.008	0.954	0.004	1.140	0.017	1.196	0.019	71.2	0.6	1.456	0.025
0.010	0.925	0.006	1.093	0.015	1.181	0.018	n.d.	n.d.	1.493	0.026
0.005	0.941	0.003	1.180	0.010	1.254	0.012	n.d.	n.d.	n.d.	n.d.
0.007	0.940	0.004	1.131	0.010	1.203	0.012	72.9	1.5	1.415	0.030
0.006	0.962	0.004	1.171	0.009	1.217	0.010	70.2	0.7	1.401	0.017
0.009	1.079	0.004	1.140	0.018	1.057	0.017	n.d.	n.d.	n.d.	n.d.
0.006	0.965	0.004	1.180	0.012	1.223	0.013	71.6	0.8	1.479	0.022
0.007	0.959	0.004	1.190	0.010	1.240	0.011	66.1	0.6	1.309	0.017
0.011	0.963	0.005	1.142	0.016	1.186	0.018	n.d.	n.d.	n.d.	n.d.
0.012	1.028	0.004	1.078	0.035	1.049	0.035	17.0	0.2	1.036	0.036
0.008	0.958	0.004	1.151	0.013	1.201	0.014	90.2	0.8	1.650	0.023
0.006	0.956	0.004	1.133	0.015	1.186	0.016	n.d.	n.d.	n.d.	n.d.
0.014	0.968	0.006	1.178	0.021	1.217	0.023	34.4	0.5	1.511	0.036
0.014	1.051	0.006	1.141	0.025	1.086	0.024	12.82	0.09	0.978	0.022
0.010	0.979	0.005	1.142	0.018	1.166	0.019	76.1	0.4	1.769	0.030
0.013	1.040	0.005	1.180	0.008	1.135	0.010	24.4	0.3	1.917	0.042

0.004	0.889	0.004	1.019	0.006	1.146	0.008	133.8	2.0	1.033	0.016
0.005	0.911	0.004	1.058	0.004	1.162	0.006	151.5	1.3	1.240	0.014
0.003	0.878	0.004	1.025	0.007	1.168	0.010	167.5	1.9	1.221	0.016
0.005	0.949	0.004	0.999	0.010	1.052	0.012	150.9	1.5	1.282	0.018
0.004	0.962	0.004	1.024	0.019	1.064	0.020	157.4	2.0	1.339	0.030
0.011	0.905	0.004	1.047	0.009	1.156	0.011	142.7	0.5	1.211	0.004
0.006	0.906	0.003	1.022	0.007	1.128	0.009	n.d.	n.d.	n.d.	n.d.
0.004	0.900	0.004	1.015	0.008	1.128	0.010	150.6	3.6	1.214	0.031
0.004	0.913	0.003	1.051	0.011	1.152	0.013	164.9	1.7	1.185	0.018
0.010	0.928	0.004	1.035	0.008	1.115	0.010	140.0	1.1	1.205	0.013
0.008	0.907	0.004	1.052	0.015	1.160	0.018	165.1	1.2	1.157	0.019
0.006	0.899	0.003	1.048	0.008	1.166	0.010	144.9	2.1	1.201	0.024
0.003	0.897	0.002	1.026	0.006	1.143	0.007	150.8	1.8	1.216	0.016
0.006	0.899	0.004	1.022	0.007	1.138	0.010	n.d.	n.d.	n.d.	n.d.
0.004	0.911	0.004	1.023	0.008	1.122	0.009	n.d.	n.d.	n.d.	n.d.
0.005	0.915	0.004	1.018	0.008	1.113	0.010	177.6	1.0	0.993	0.010
0.005	0.900	0.003	1.022	0.011	1.135	0.013	148.2	1.4	1.256	0.019
0.005	0.903	0.004	1.033	0.007	1.144	0.009	151.6	1.1	1.277	0.012
0.003	0.878	0.003	1.039	0.008	1.184	0.010	149.7	1.5	1.272	0.017
0.005	0.903	0.004	1.033	0.008	1.144	0.010	n.d.	n.d.	n.d.	n.d.
0.004	0.918	0.002	1.033	0.010	1.125	0.011	143.4	1.3	1.233	0.016
0.011	0.905	0.005	1.037	0.009	1.146	0.012	118.9	1.2	1.369	0.018
0.004	0.906	0.002	1.048	0.006	1.157	0.007	215.3	2.6	1.120	0.015
0.004	0.906	0.002	1.024	0.006	1.130	n.d.	n.d.	n.d.	n.d.	n.d.
0.008	0.924	0.004	1.016	0.009	1.099	0.011	90.8	1.0	1.182	0.017
0.011	0.930	0.005	0.957	0.008	1.029	0.010	41.5	0.7	1.042	0.019
0.009	0.941	0.004	1.049	0.010	1.114	0.011	n.d.	n.d.	n.d.	n.d.
0.006	0.915	0.003	1.034	0.008	1.131	0.009	110.1	2.2	1.171	0.025

0.008	0.908	0.004	1.037	0.016	1.142	0.018	36.3	0.6	1.490	0.033
n.d.	0.948	0.005	1.068	0.015	1.127	0.017	13.0	0.2	1.065	0.020
0.006	0.934	0.004	1.064	0.009	1.139	0.010	43.8	0.6	1.194	0.019
0.004	0.851	0.003	1.089	0.010	1.278	0.013	76.7	1.0	1.061	0.018
n.d.	1.008	0.004	1.007	0.025	0.999	0.026	9.9	0.1	1.339	0.038
0.030	0.983	0.007	1.125	0.012	1.144	0.015	24.8	0.2	1.111	0.016
0.007	1.090	0.006	1.088	0.008	0.998	0.009	3536.00	28.00	0.991	0.015

684

685

686
687

Table 2. Mineral/melt partition coefficients and mineral modes used in melting model calculations

Lithology	D_U	D_{Th}	Mineral mode	Data source
Spinel peridotite:				
olivine	0.00005	0.00047	0.53	Salters et al. (2002)
orthopyroxene	0.0024	0.0027	0.14	Salters et al. (2002)
clinopyroxene	0.008	0.007	0.30	Salters et al. (2002)
Garnet peridotite:				
olivine	0.00005	0.00047	0.59	Salters et al. (2002)
orthopyroxene	0.0078	0.0086	0.21	Salters et al. (2002)
clinopyroxene	0.003	0.004	0.08	Salters et al. (2002)
garnet	0.038	0.017	0.12	Salters et al. (2002)
Eclogite:				
clinopyroxene	0.0041	0.0032	0.75	Pertermann et al. (2004)
garnet	0.024	0.0042	0.25	Pertermann et al. (2004)
Garnet pyroxenite:				
clinopyroxene	0.017	0.015	0.60	Pertermann et al. (2004)
garnet	0.013	0.0032	0.40	Pertermann et al. (2004)

688
689

Figure

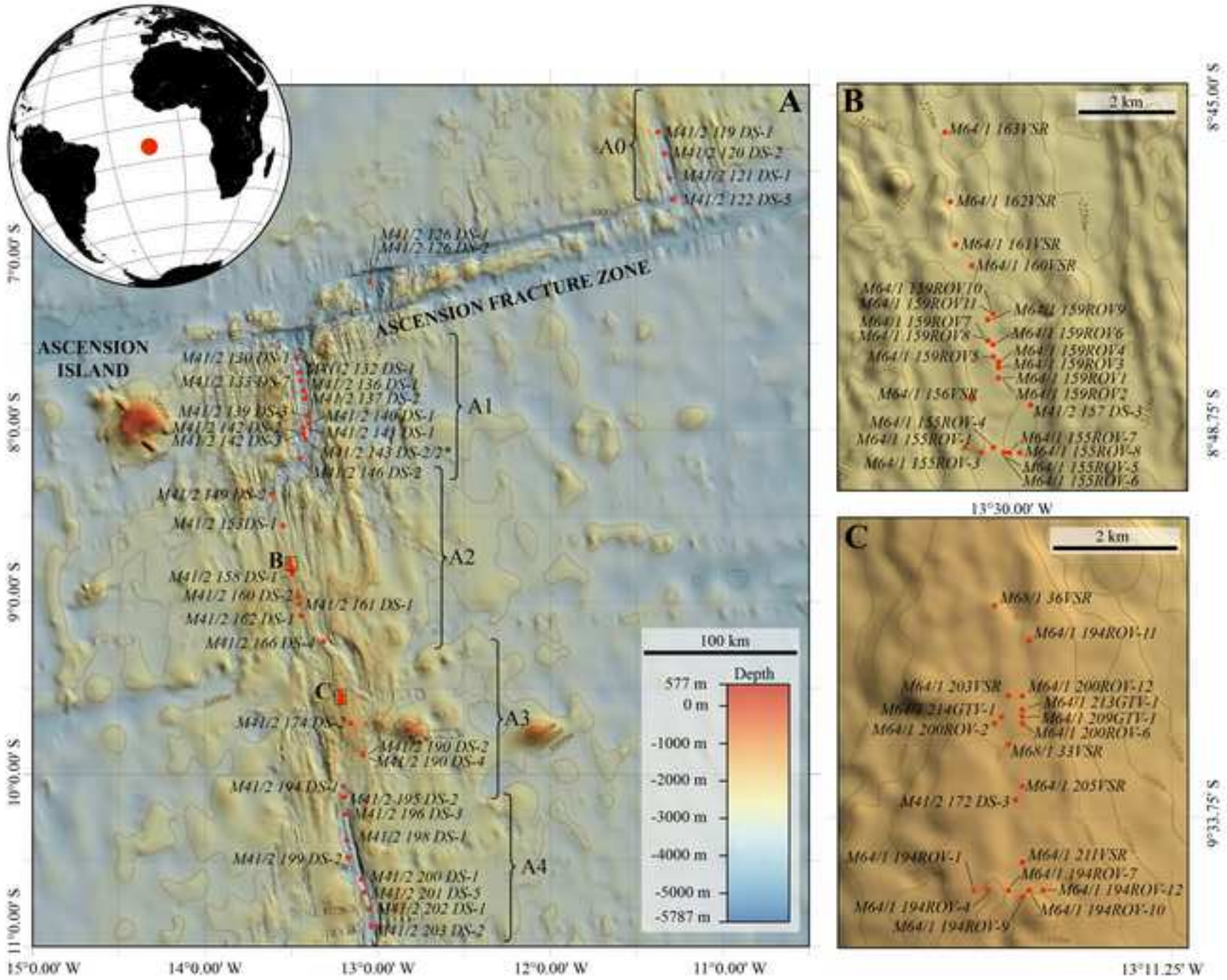

Figure

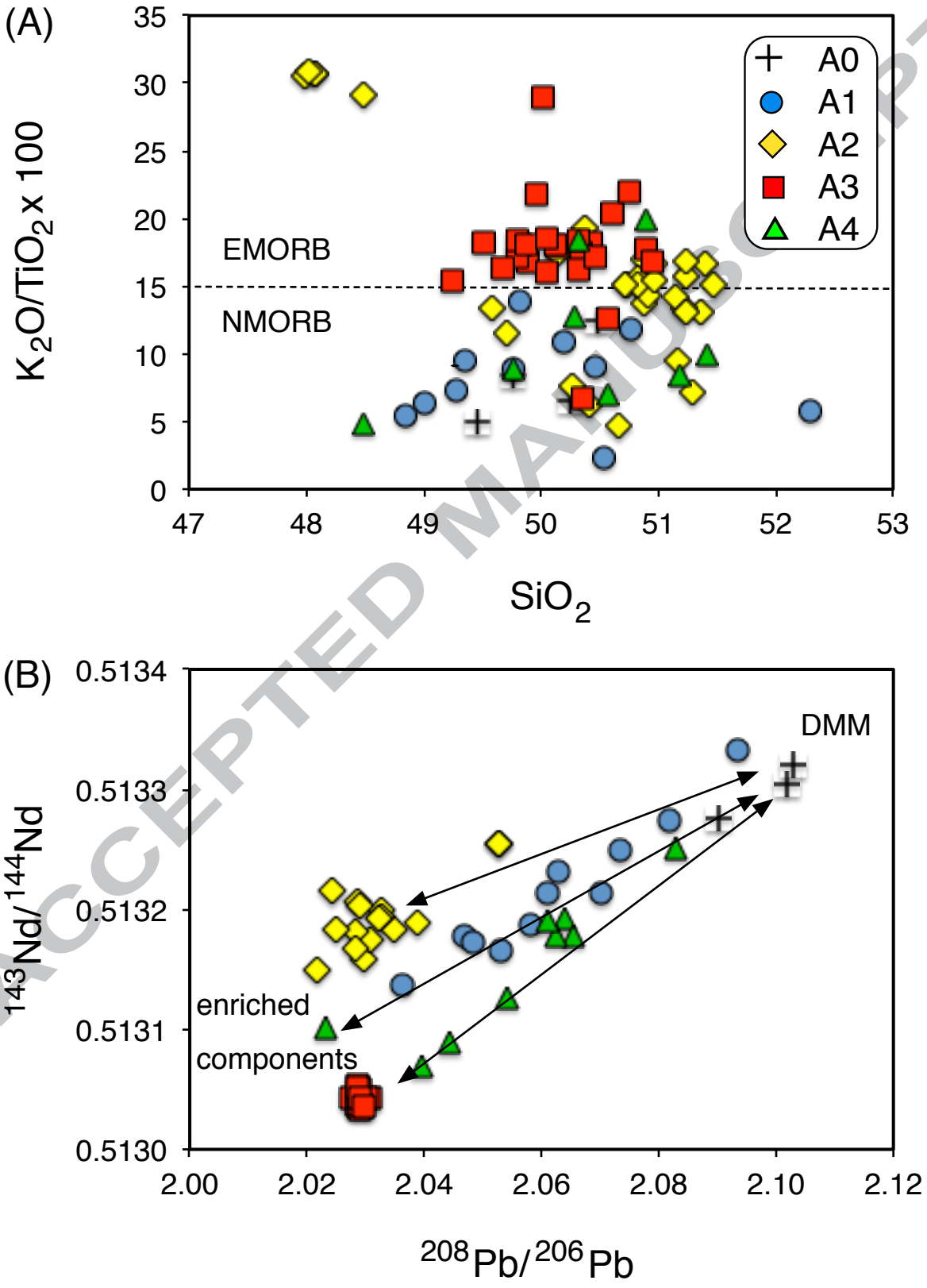

Figure

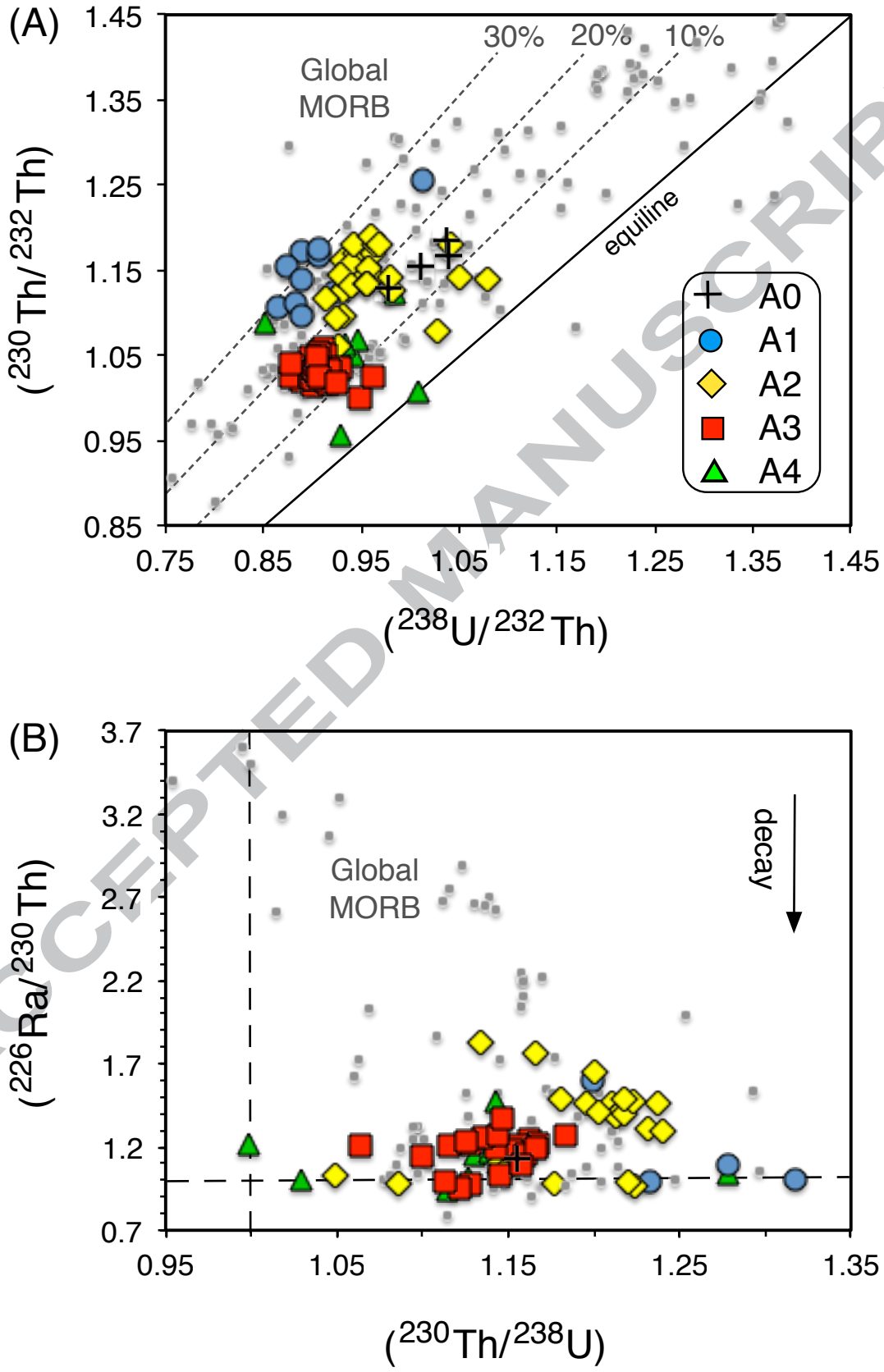

Figure

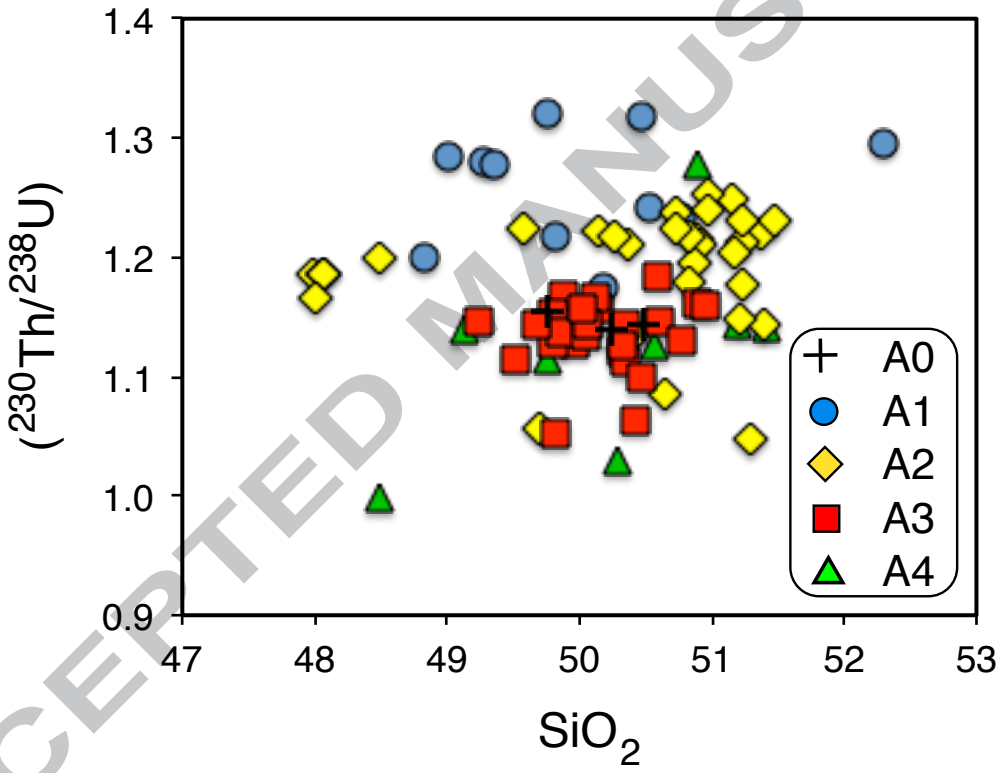

Figure

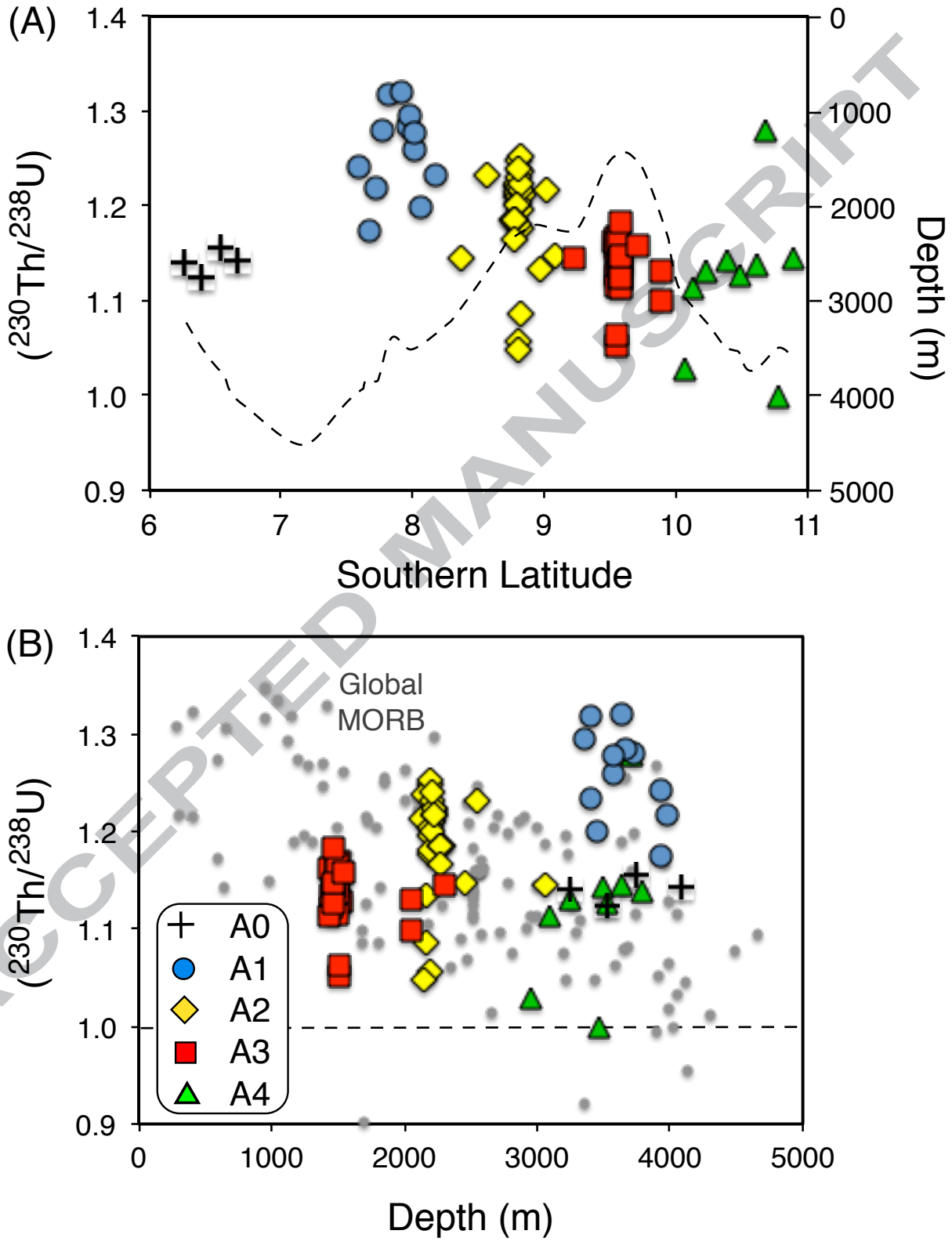

Figure

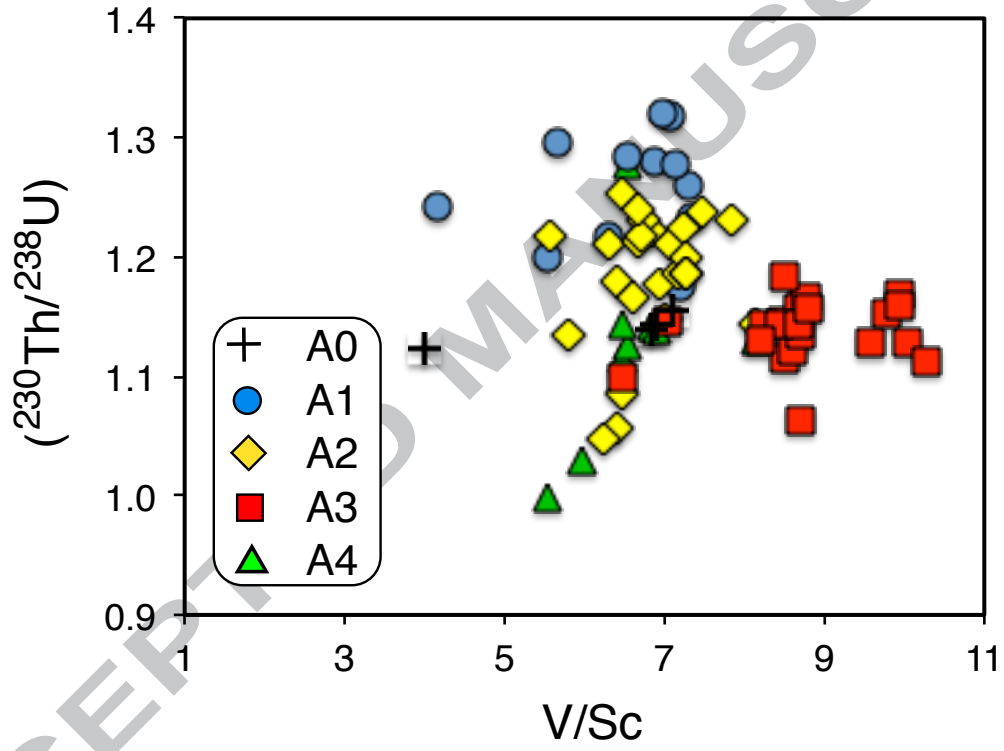

Figure

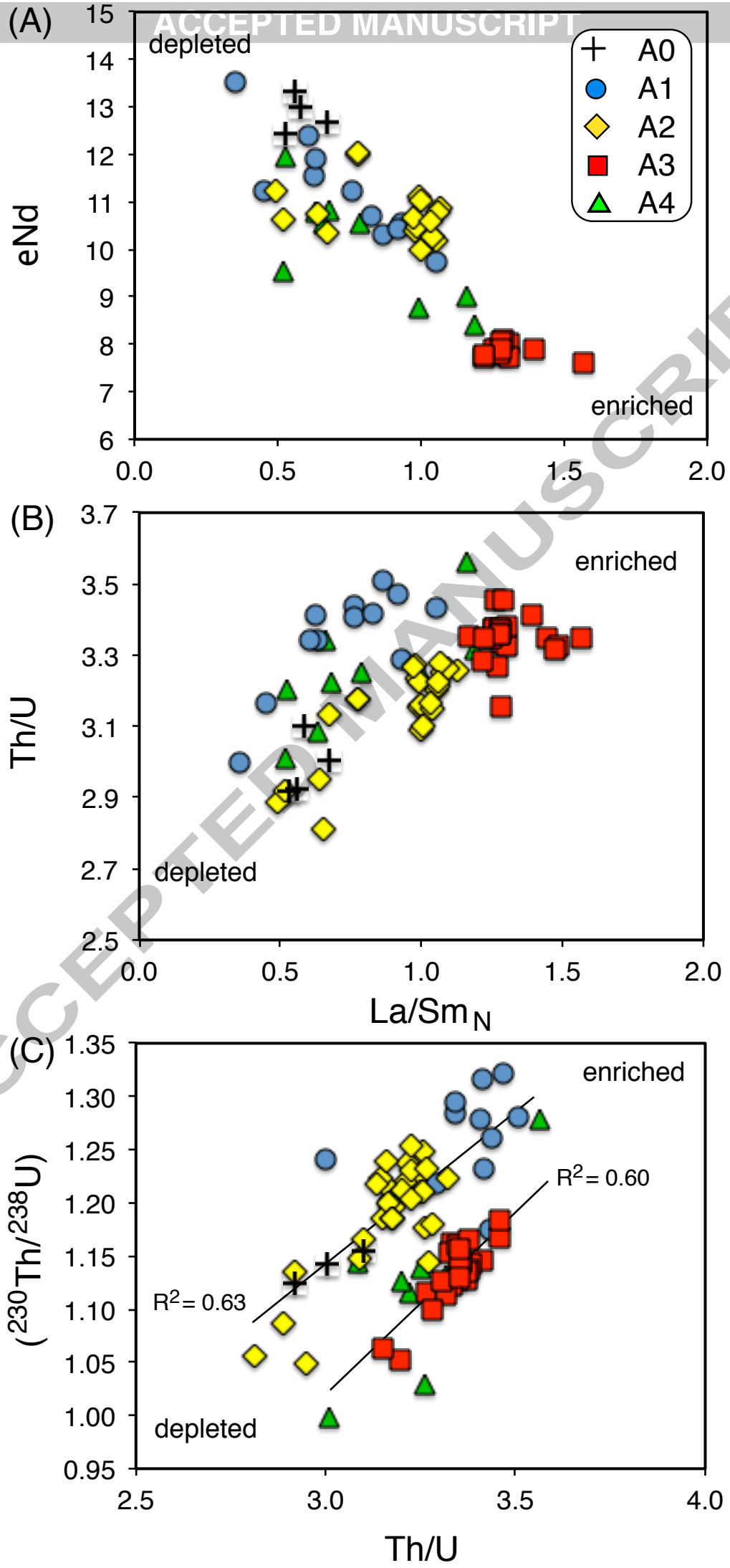

Figure

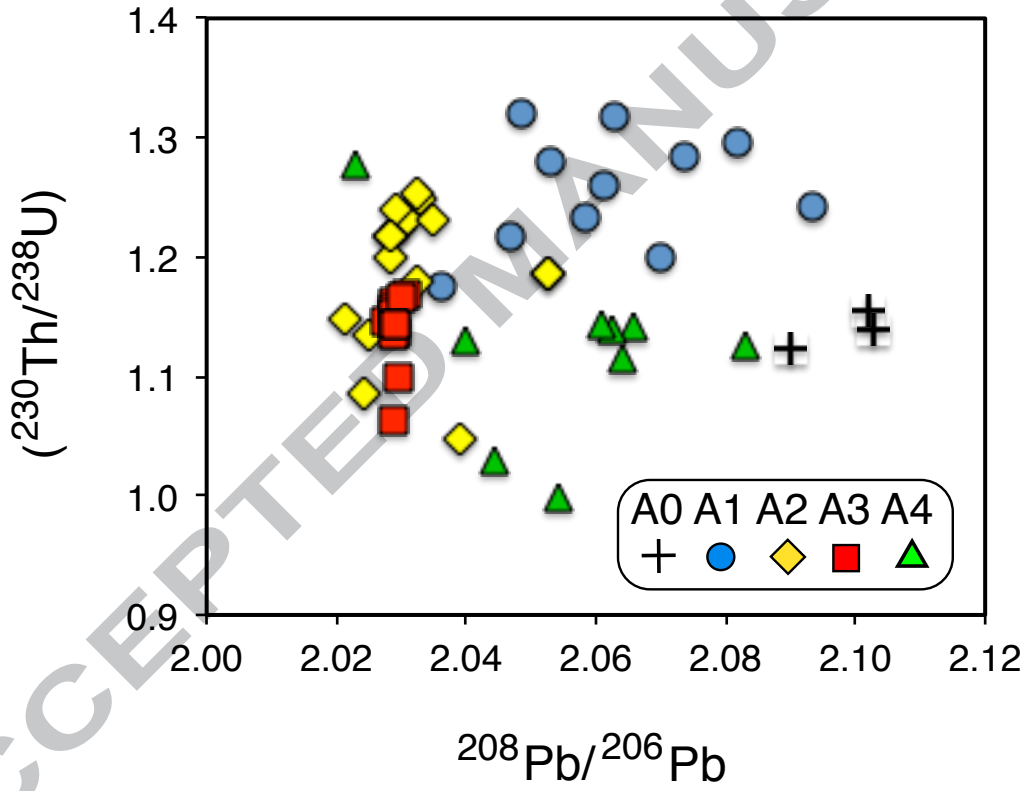

Figure